Zero to ultralow magnetic field NMR of [1-^{13}C]pyruvate and [2-^{13}C]pyruvate enabled by SQUID sensors and hyperpolarization

John Z. Myers [1,*] Friedemann Bullinger,[2,*] Nicolas Kempf [2] Markus Plaumann [3] Adam Ortmeier [4,5]
Thomas Theis [4,5] Pavel Povolni [2] Jannik Romanowski [2] Jörn Engelmann,[2] Klaus Scheffler,[2,6] Jan-Bernd Hövener,[7]
Kai Buckenmaier,[2,†] Rainer Körber [1,‡] and Andrey N. Pravdivtsev [7,§]

[1]*Physikalisch-Technische Bundesanstalt (PTB), Abbestraße 2–12, 10587 Berlin, Germany*
[2]*High-Field Magnetic Resonance Center, Max Planck Institute for Biological Cybernetics, Max-Planck-Ring 11, 72076 Tübingen, Germany*
[3]*Institute of Molecular Biology and Medicinal Chemistry, Medical Faculty, Otto-von-Guericke University Magdeburg, Leipziger Str. 44, 39120 Magdeburg, Germany*
[4]*Department of Chemistry, North Carolina State University, Raleigh, North Carolina 27695, USA*
[5]*Department of Physics, North Carolina State University, Raleigh, North Carolina 27695, USA*
[6]*Department of Biomedical Magnetic Resonance, Eberhard-Karls University, 72076 Tübingen, Germany*
[7]*Section Biomedical Imaging, Molecular Imaging North Competence Center (MOIN CC), Department of Radiology and Neuroradiology, University Medical Center Schleswig-Holstein and Kiel University, Am Botanischen Garten 14, 24118 Kiel, Germany*

Accurately characterizing magnetic resonance of molecules at zero to ultralow magnetic field (nTs-µTs) is challenging, due to vanishingly small sensitivity, which depends on the thermal equilibrium polarization of the nuclear spins and instrumentation. We overcome the former limitation with the parahydrogen-based hyperpolarization method SABRE-SHEATH (signal amplification by reversible exchange in shield enables alignment transfer to heteronuclei). This method allows for the continuous transfer of spin order from parahydrogen to a substrate via chemical exchange, reaching polarization levels of some percent (level equivalent to ^{13}C polarization at 20 kT). We address the latter with our application of a superconducting quantum interference device (SQUID)-based detector setup that allows for broadband detection (dc-MHz) with exquisite sensitivity over its entire range. Here, we present the results of our comprehensive characterization of [1-^{13}C]pyruvate and [2-^{13}C]pyruvate, hyperpolarized via SABRE-SHEATH, from zero field to 100 µT. To this end, we show low-noise, high-resolution spectra for both molecules, detecting how the NMR spectrum changes from the *J*-coupling dominated zero-field spectrum to the strongly coupled spectrum, and then finally to the conventional high-field, otherwise known Zeeman-dominated spectrum. We also analytically derive the evolution of product operators in arbitrary magnetic fields, which aid in the understanding of the differences between spin evolution and spin-coupling regimes. We predict and confirm that the absence of spin precession at zero field can result in observable oscillation of magnetization along one axis with a frequency of the *J*-coupling constant, no observable spin evolution, or observing spin evolution that corresponds to "forbidden" transitions at high field. The zero-field spectra with their near-dc signals reveal different relaxation rates for the different spin states of hyperpolarized ^{13}C pyruvates, demonstrating the utility of SQUID detectors and hyperpolarization for the characterization of magnetic resonance phenomena.

I. INTRODUCTION

Nuclear magnetic resonance (NMR) has become an indispensable analytical tool with numerous applications in physics, chemistry, industry, and medicine [1,2]. Since the time of its development, the mainstream path has been to make stronger magnets, currently culminating at 28.2 T (1.2-GHz ^{1}H frequency) for commercial systems [3] and even higher in pulsed-field systems [4]. Higher magnetic fields result in higher polarization and, thus, a larger signal-to-noise ratio (SNR).

During the last decade, an opposite trend has also developed: benchtop NMR systems with modest 1–2-T permanent magnets have substituted for expensive, high-resolution, cryogenic NMR systems, in some areas becoming industry standards. Zero- and ultralow field (ZULF) NMR have also become possible, combining developments in nuclear-spin hyperpolarization and highly sensitive, broadband, direct current (dc) magnetometers [5–7]. Even though ZULF NMR has

*These authors contributed equally to this work.
†Corresponding author: kai.buckenmaier@tuebingen.mpg.de
‡Corresponding author: rainer.koerber@ptb.de
§Corresponding author: andrey.pravdivtsev@rad.uni-kiel.de
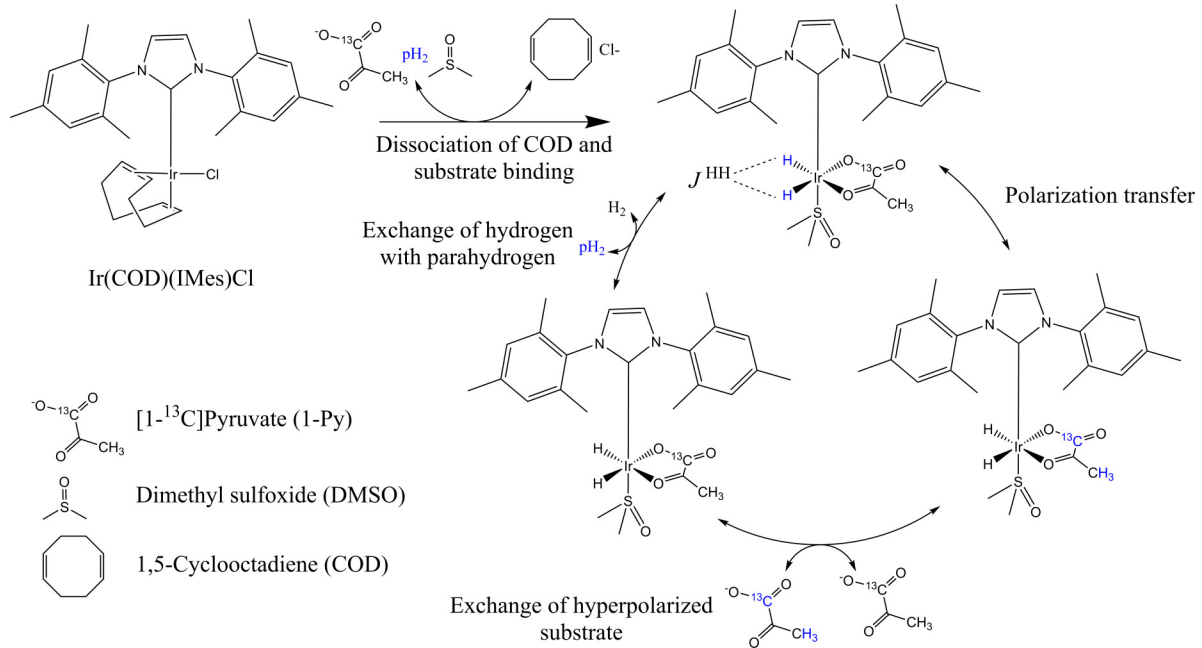
FIG. 1. Schematic representation of the SABRE effect on 1-Py. Parahydrogen (pH$_2$) and 1-Py with its coligand dimethyl sulfoxide (DMSO) transiently bind to the Ir-IMes complex, forming a spin-spin coupled system. At appropriate magnetic fields (100s of nT), the spin order of pH$_2$ is converted into polarization of the ^{1}H and ^{13}C nuclei on the pyruvate molecule, as highlighted in blue. All steps with the activated catalyst [after dissociation of cyclooctadiene (COD)] are fully reversible, regenerating their initial reactants with each cycle, enabling SABRE to be performed continuously on samples on the timescale of hours.

no chemical shift resolution, *J*-coupling topology and selective hyperpolarization still enable differentiation of chemical structures, supporting its wider use [8–10]. However, its use does require that nuclear spins be prepolarized in one way or another. One method is via hyperpolarization techniques, which populate nuclear-spin states far beyond thermal equilibrium levels, manifesting in strongly increased NMR signals [11–13]. Interestingly, samples implanted with polarized muons have been also successfully probed at ZULF conditions [14].

We demonstrate NMR spectroscopy from zero (≈ 1 nT) to 1 μT, measured using a dc superconducting quantum interference device (SQUID) sensor [15]. For signals from near dc (<1 Hz) up to $\sim$MHzs, SQUID sensors offer superior sensitivity compared to conventional Faraday coils [16,17]. Faraday coils in contrast have increased sensitivity with frequency, becoming more advantageous at high frequencies. While optically pumped magnetometers (OPM) are another alternative to SQUIDs, they have a worse noise performance at low frequencies [18–20]. Additionally, SQUIDs act as broadband detectors allowing simultaneous observation over their entire frequency range.

For this work, we used signal amplification by reversible exchange (SABRE) [12] hyperpolarization to prepolarize nuclear spins. SABRE offers exceptionally high ^{1}H [21] polarization at mT fields, and the variant, SABRE in shield enables alignment transfer to heteronuclei (SABRE-SHEATH), offers ^{13}C [22–25] and ^{15}N polarization up to the order of percent at μT magnetic fields [26,27].

In SABRE, pyruvate, an Ir-IMes catalyst [28], and parahydrogen (pH$_2$) produce a short-lived complex, whose spin-spin interactions allow the transfer of spin order from pH$_2$ to pyruvate (Fig. 1). This polarization transfer is possible at sufficiently low magnetic fields, where the ^{1}H atoms from pH$_2$ and the ^{13}C nucleus of pyruvate are strongly coupled. Optimum fields for the polarization transfer to a pyruvate ^{13}C-labeled nucleus were found to be between 300–500 nT, around the estimated energy-level anticrossing (LAC) of this system [26,29]: $B_{\text{LAC}} = \frac{2\pi J^{\text{HH}}}{\gamma^{1}\text{H} - \gamma^{13}\text{C}} \sim 330$ nT for J^{HH} of -10.5 Hz, where γ is the gyromagnetic ratio. The higher experimentally found optima are attributed to rapid chemical exchange [30–33].

Hyperpolarization generated with SABRE-SHEATH of [1-^{13}C]pyruvate (1-Py) and [2-^{13}C]pyruvate (2-Py) has recently been shown to be ample enough for *in vivo* metabolic imaging studies at high field [34,35]. It also generates sufficient signal amplitude to measure, with high sensitivity and resolution, NMR spectra from zero to 1 μT, allowing for characterization at ZULF. Over increasing magnetic field, we have observed how the spectra changes: at zero field, the NMR spectrum is dominated by *J* coupling [36–40], with increasing field, the lines move apart and additional signals are observed, and at 1 μT and higher, the ^{1}H and ^{13}C signals of pyruvate begin to resemble high-field spectra, becoming dominated by Zeeman interactions.

Because NMR spectroscopy is well characterized at high magnetic fields, we will first describe NMR transition frequencies from high to low magnetic fields. We will then derive a general solution for the NMR spectrum of the magnetized two spin-1/2 system and transition frequencies for other
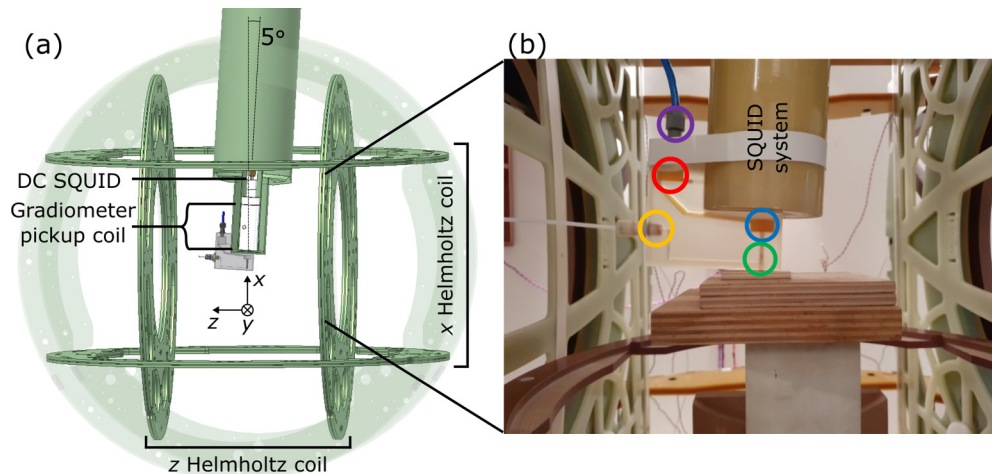
FIG. 2. Field-switching ZULF setup. (a) Schematic of the SQUID ZULF setup without rf excitation at the PTB showing the Helmholtz coils generating B_{hyp}^x along the x and B_{det}^z along the z axis. A first-order, axial gradiometer coupled to the SQUID enables signal acquisition along the x axis (acq_x). The position of the SABRE reactor is also shown, along with an inside view of the measurement system, showing both the single-order gradiometer pick-up coil and the dc SQUID within the low-noise helium dewar LINOD2. The SQUID system is tilted slightly by $\sim 5°$ with respect to the x axis to aid backflow of the SABRE sample within the reactor. (b) Picture of the setup corresponding to the indicated region from (a). In orange is the pH_2 inlet into the SABRE reactor; green is the Kenics static mixer, blue is the principal sample volume, red is the overflow receptacle and purple is the pH_2 outlet.

multispin systems. Finally, we will compare this analysis with observed zero and ultralow field NMR experiments of hyperpolarized 1-Py and 2-Py.

II. METHODS

A. ZULF experiments using SQUID sensors without rf excitation

The system, located at the Physikalisch-Technische Bundesanstalt (PTB) in Berlin, was used to acquire high resolution MR spectra. A close-up shot of the setup at the PTB is shown in Fig. 2. For signal detection, an ultrasensitive SQUID system was used. It consisted of a first-order axial gradiometer inductively coupled to a current-sensing SQUID for data acquisition along the x axis (acq_x). The diameter of the pick-up coil was 45 mm with a baseline of 120 mm. The probe was operated in the liquid helium dewar LINOD2 [41], which features negligible magnetic noise, reaching a white-noise level of ~ 200 aT/$\sqrt{Hz}$. The SQUID system was located inside a three-axis ULF magnetic resonance imaging (MRI) coil system. The whole setup was operated in the moderately magnetically shielded room "ZUSE MSR" (two layers of μ-metal and one eddy-current shield), achieving residual fields of < 1.5 nT after degaussing [42].

For high-resolution ZULF spectroscopy, separate Helmholtz coils were used to generate the SABRE-SHEATH field, B_{hyp}^x, and the read field, B_{det}^z. The SHEATH field B_{hyp}^x was oriented along the x direction with a range of zero to ~ 1.3 μT. To induce precession, a nonadiabatic switch to the observation field, B_{det}^z, along the z direction was performed (note that the superscripts of field variables define the direction of their corresponding fields).

B. ZULF experiments using SQUID sensors with rf excitation

Some experiments were carried out on a different system located at the Max Planck Institute (MPI) in Tübingen, which

has been detailed before [15]. An illustration is presented in the Supplemental Material (SM), Fig. S2 [43].

C. Simulations of NMR spectra

NMR spectra were simulated using the density-matrix approach and the numerical solution of the Liouville–von Neumann equation [Eq. (4)] of the liquid-state Hamiltonian for 1-Py and 2-Py, which included three protons and one ^{13}C nuclei. The relevant J-coupling constants used were J^{CH} of 1.27 and 6 Hz for 1-Py and 2-Py, respectively. The orientation of the magnetic field and observation axis were varied to fit experimental data. The relaxation was treated phenomenologically by multiplying the measured expectation values (signal) by an exponentially decaying function $\exp(-Rt)$, where R is a relaxation constant. Using Redfield relaxation theory, we also included the effect of more explicit relaxation mechanisms, such as intramolecular dipole-dipole relaxation [44–46].

D. Simulations of SABRE field dependence

We simulated polarization transfer and chemical exchange, using a SABRE model detailed before [31,47]. The difference here is that we do not have to assume that two substrates dissociate simultaneously. Since only one substrate (pyruvate) exchanges here, this results in a theory with fewer assumptions, compared to other SABRE experiments with two exchanging ligands [12,31,47]. The relevant J-coupling constants used for simulations of 1-Py [Fig. 5(c)] are $J^{HH} = -10.48$ Hz, with the two ^{1}H-^{13}C interactions being 0 and 0.55 Hz, implying the polarization transfer mechanism, as shown in complex **C-I** [Fig. 5(e)]. The constants for 2-Py [Fig. 5(d)] are $J^{HH} = -6.55$ Hz, with the two ^{1}H-^{13}C interactions being -2.69 and 0.41 Hz, implying the polarization transfer mechanism, as shown in complex **C-II**

[Fig. 5(f)] [48]. The important characteristic of these complexes is lifetime; the inverse value of lifetime, the dissociation exchange rate, k_d, was the fitting parameter.

E. Sample preparation

The sample consisted of approximately 50 mM 1-Py (sodium pyruvate-1-^{13}C, Sigma-Aldrich 490709) or 50 mM 2-Py (sodium pyruvate-2-^{13}C, Sigma-Aldrich 490725) with 5 mM IrIMes (synthesized following Ref. [49]), and 18 mM DMSO (Sigma-Aldrich), dissolved in 8 mL methanol (Roth, Rotisolv $\geqslant$99.9%). Using a home-built, liquid-helium dipstick, we prepared nominally 99% pH$_2$. We activated the catalyst by bubbling it into the reaction chamber at ambient pressure at a flow rate of 1 L/h for half an hour. Prior to performing detection, we bubbled pH$_2$ for 40 s into the reaction chamber at ambient pressure at a flow rate of 2 L/h. During detection, the flow was shunted away from the reactor and the magnetic field nonadiabatically switched. Over an experiment, the sample concentrations changed slowly during the measurement times as the methanol evaporated.

F. Data acquisition and analysis

Signal acquisition was performed over 40 s, sampling at 20 kHz (80 000 points) (NI PXI 4462). Data were baseline corrected in the time domain by demeaning the data and applying a five-term polynomial fit to the last 20 s of the data to account for magnetic-field drift within the ZUSE MSR. A Fourier transform was then performed on the data, zero padded to the length of the third-closest, higher power of 2. First-order phasing was performed to eliminate dephasing of the ^{13}C and ^{1}H signals from one another using the dead time between nonadiabatic field switching and data acquisition. Zeroth-order phasing was then applied by maximizing symmetry over the phasing window.

Linewidth and initial amplitude analysis were performed on zero-field data with only zeroth-order phasing by applying a Lorentzian fit to the data in the frequency domain.

III. RESULTS AND DISCUSSION

Numerical simulations of the zero-field (ZF) and ultralow-field (ULF) spectra are well described by Stern and Sheberstov [50], whereas here, we will mainly focus on the analytical analysis of spin dynamics at ZULF conditions.

First, we will find the NMR spectra for the two spins-1/2 system (AX system) at arbitrary magnetic field (note that if spins in the system are listed without superscript, spins-1/2 are assumed). Then, we will explain how this system can be used to describe the NMR spectra of 1-Py and 2-Py, both having A_3X-type spin systems. Afterwards, we will show spectra of SABRE-SHEATH hyperpolarized 1-Py and 2-Py at ZULF and discuss some of the implications.

A. NMR spectra of the two spins-1/2 system at an arbitrary magnetic field

The system of two nuclear spins-1/2 in a liquid state for B_0 aligned only along the z axis is given by the following Hamiltonian:

$$
\begin{aligned}
\hat{H}^{AX} &= -\nu^A \hat{I}_z^A - \nu^X \hat{I}_z^X + J(\hat{\mathbf{I}}^A \cdot \hat{\mathbf{I}}^X) \\
&= -\frac{\Sigma\nu}{2}(\hat{I}_z^A + \hat{I}_z^X) - \frac{\delta\nu}{2}(\hat{I}_z^A - \hat{I}_z^X) + J(\hat{\mathbf{I}}^A \cdot \hat{\mathbf{I}}^X),
\end{aligned} \quad (1)
$$

where $\nu^j = \frac{\gamma^j B_0}{2\pi}(1 + \delta_j)$ is the linear Larmor precession frequency of spin j; $j = A$ or X; $\Sigma\nu = \nu^A + \nu^X$; $\delta\nu = \nu^A - \nu^X$; γ is the gyromagnetic ratio; δ_j is the chemical shift; J is the constant of scalar spin-spin coupling, and $\hat{\mathbf{I}}^A$ and $\hat{\mathbf{I}}^X$ are the vectors of nuclear-spin operators for spins A and X (note that the Hamiltonian is defined in the units of Hz). One can easily find the energy levels and eigenstates of this Hamiltonian to be

$$
E_1^{AX} = -\frac{\Sigma\nu}{2} + \frac{J}{4}, \quad |1\rangle = |\alpha\alpha\rangle = |T_+\rangle
$$

$$
E_2^{AX} = -\frac{J}{4} - \frac{1}{2}\sqrt{\delta\nu^2 + J^2}, \quad |2\rangle = \cos\theta|\alpha\beta\rangle - \sin\theta|\beta\alpha\rangle = \cos\left(\theta + \frac{\pi}{4}\right)|T_0\rangle + \sin\left(\theta + \frac{\pi}{4}\right)|S\rangle
$$

$$
E_3^{AX} = -\frac{J}{4} + \frac{1}{2}\sqrt{\delta\nu^2 + J^2}, \quad |3\rangle = \sin\theta|\alpha\beta\rangle + \cos\theta|\beta\alpha\rangle = \sin\left(\theta + \frac{\pi}{4}\right)|T_0\rangle - \cos\left(\theta + \frac{\pi}{4}\right)|S\rangle
$$

$$
E_4^{AX} = \frac{\Sigma\nu}{2} + \frac{J}{4}, \quad |4\rangle = |\beta\beta\rangle = |T_-\rangle,
$$

$$
\tan(2\theta) = \frac{J}{\nu^A - \nu^X} = \frac{J}{\delta\nu}. \quad (2)
$$

Here, we have used the standard notation of nuclear-spin states $|\alpha\rangle$ and $|\beta\rangle$ to refer to the states of spin-1/2 parallel or antiparallel to the magnetic field. The Zeeman basis (ZB) consists of four states, ZB $=(|\alpha\alpha\rangle, |\alpha\beta\rangle, |\beta\alpha\rangle$, and $|\beta\beta\rangle)$. This is a good basis at high magnetic fields, where $\Sigma\nu \gg J$,

since it is a good approximation of the eigenstates of the Hamiltonian in this case. In contrast, a good basis at low magnetic fields, when two spins are strongly coupled, $\Sigma\nu \ll J$, is the singlet-triplet basis, STB $=(|T_+\rangle = |\alpha\alpha\rangle, |S\rangle = \frac{|\alpha\beta\rangle - |\beta\alpha\rangle}{\sqrt{2}}$, $|T_0\rangle = \frac{|\alpha\beta\rangle + |\beta\alpha\rangle}{\sqrt{2}}$, and $|T_-\rangle = |\beta\beta\rangle)$.

High-field and ZULF approximations, when evaluating these eigenstates, show how these arbitrary eigenvalues and eigenstates correlate with their high-field and ZULF approximations. If $\delta\nu > 0$ and $J > 0$ then $0 \leqslant \theta \leqslant \frac{\pi}{4}$ and at zero fields $\theta \overset{B_0 \to 0}{\to} \frac{\pi}{4}$, $E_2^{AX} \to = -\frac{3J}{4}$, $|2\rangle \to |S\rangle$, $E_3^{AX} \to \frac{J}{4}$, and $|3\rangle \to |T_0\rangle$, whereas at high fields $\theta \overset{B_0 \to +\infty}{\to} 0$, $E_2^{AX} \to -\frac{J}{4} - \frac{1}{2}\delta\nu$, $|2\rangle \to |\alpha\beta\rangle$, $E_3^{AX} = -\frac{J}{4} + \frac{1}{2}\delta\nu$, and $|3\rangle \to |\beta\alpha\rangle$.

We have selected the order of the eigenstates to coincide with that of the states in the ZB at high magnetic fields (note that typically, product operators, e.g., $\hat{\text{I}}_z^A$ and $\hat{\text{I}}_z^X$ in textbooks are often defined in the ZB). All product operators used within this paper are listed in Table S1 [43].

In high-field (HF) NMR, only single quantum coherences are observed, which results in only four "allowed" transitions for the AX system with the following transition frequencies,

$\nu_{k \to l} = E_k - E_l$:

$$\nu_{2 \to 1} = \frac{\Sigma\nu}{2} - \frac{J}{2} - \frac{1}{2}\sqrt{\delta\nu^2 + J^2} \to \begin{cases} \overset{B_0 \to +\infty}{\to} \nu_{\alpha\beta \to \alpha\alpha} \approx \nu^X - \frac{J}{2} \\ \overset{B_0 \to 0}{\to} \nu_{S \to T_+} \approx -\left(J - \frac{\Sigma\nu}{2}\right) \end{cases}$$

$$\nu_{3 \to 1} = \frac{\Sigma\nu}{2} - \frac{J}{2} + \frac{1}{2}\sqrt{\delta\nu^2 + J^2} \to \begin{cases} \overset{B_0 \to +\infty}{\to} \nu_{\beta\alpha \to \alpha\alpha} \approx \nu^A - \frac{J}{2} \\ \overset{B_0 \to 0}{\to} \nu_{T_0 \to T_+} \approx \frac{\Sigma\nu}{2} \end{cases}$$

$$\nu_{4 \to 2} = \frac{\Sigma\nu}{2} + \frac{J}{2} + \frac{1}{2}\sqrt{\delta\nu^2 + J^2} \to \begin{cases} \overset{B_0 \to +\infty}{\to} \nu_{\beta\beta \to \alpha\beta} \approx \nu^A + \frac{J}{2} \\ \overset{B_0 \to 0}{\to} \nu_{T_- \to S} \approx J + \frac{\Sigma\nu}{2} \end{cases}$$

$$\nu_{4 \to 3} = \frac{\Sigma\nu}{2} + \frac{J}{2} - \frac{1}{2}\sqrt{\delta\nu^2 + J^2} \to \begin{cases} \overset{B_0 \to +\infty}{\to} \nu_{\beta\beta \to \beta\alpha} \approx \nu^X + \frac{J}{2} \\ \overset{B_0 \to 0}{\to} \nu_{T_- \to T_0} \approx \frac{\Sigma\nu}{2} \end{cases}$$

$$\nu_{3 \to 2} = \sqrt{\delta\nu^2 + J^2} \to \begin{cases} \overset{B_0 \to +\infty}{\to} \nu_{\beta\alpha \to \alpha\beta} \approx \delta\nu \\ \overset{B_0 \to 0}{\to} \nu_{T_0 \to S} \approx J \end{cases}. \tag{3}$$

Here, the ZULF and high-field limits are shown in addition to the fifth $\nu_{3 \to 2}$ frequency of the HF zero-quantum or "flip-flop" forbidden transition $|\beta\alpha\rangle \to |\alpha\beta\rangle$. Of note, for positive J, only $\nu_{2 \to 1}$ can become zero at $B > 0$. This happens when $\Sigma\nu^2 - 2\Sigma\nu J = \delta\nu^2$ or $B = \pi \frac{\gamma^A + \gamma^X}{\gamma^A \gamma^X} J$, which explains why $\nu_{S \to T_+}$ is negative.

There are four principal ZULF frequencies: $\frac{\Sigma\nu}{2}$, J, and $J \pm \frac{\Sigma\nu}{2}$ and four frequencies at the HF limit: $\nu^A \pm \frac{J}{2}$ and $\nu^X \pm \frac{J}{2}$. While the transition $3 \to 2$ is normally forbidden at HF, it is allowed at ZULF at the frequency J.

One can find the transition amplitudes using Fermi's golden rule [19]. However, we have attempted to develop a product-operator approach for the ZULF case instead. Since modern NMR spectrometers observe free-induction decay (FID) signal, induced by the precession of magnetization, we believe it more instructive to use a product-operator approach, since the Fermi rule is better suited to spectroscopy, based on continuous wave sweeping.

The evolution of the spin system can be described using the Liouville–von Neumann equation:

$$\frac{d\hat{\rho}}{dt} = -i2\pi[\hat{H}, \hat{\rho}]. \tag{4}$$

Here, we have added 2π to compensate for defining the Hamiltonian in Hz. The solution for this equation is straightforward when the density matrix $\hat{\rho}$ is written in the eigenbasis of the Hamiltonian (note that the first index refers to the row and the second to the column of the corresponding matrices):

$$\rho_{kk}(t) = \rho_{kk}(t = 0)$$
$$\rho_{kl}(t) = e^{-2\pi i\nu_{k \to l}}\rho_{kl}(t = 0), \ k \neq l. \tag{5}$$

Using these equations, one can derive the evolution of the spin system. At the HF approximation, the popular approach is the product-operator formalism [51], which is very tricky at ZULF conditions due to factors such as no longer being able to assume weak coupling in comparison to Zeeman interactions.

First, let us assume that the magnetic field is along the z axis and that the system of two spins, AX, was prepared such that magnetization along the x axis (transversal component) and z axis (longitudinal component) is generated. The following density matrix gives the state of such a spin system:

$$\hat{\rho}(t = 0) = \frac{\hat{1}}{4} + \frac{1}{2}\left(p_x^A \hat{I}_x^A + p_x^X \hat{I}_x^X + p_z^A \hat{I}_z^A + p_z^X \hat{I}_z^X\right), \tag{6}$$

where p is the polarization for a given nucleus along a given axis. From now on, superscripts refer to the label of the spin, and subscripts to its Cartesian coordinates. By rotation around the z axis, one can always adjust the x axis to be aligned with the transversal component of magnetization.

Then, under the action of the Hamiltonian [Eq. (1)], using Eq. (5), one can derive the evolution of all elements of the density matrix [Eq. (6)] at an arbitrary magnetic field [Eq. (S13), SM [43]]. The corresponding evolution of the product operators for spin A
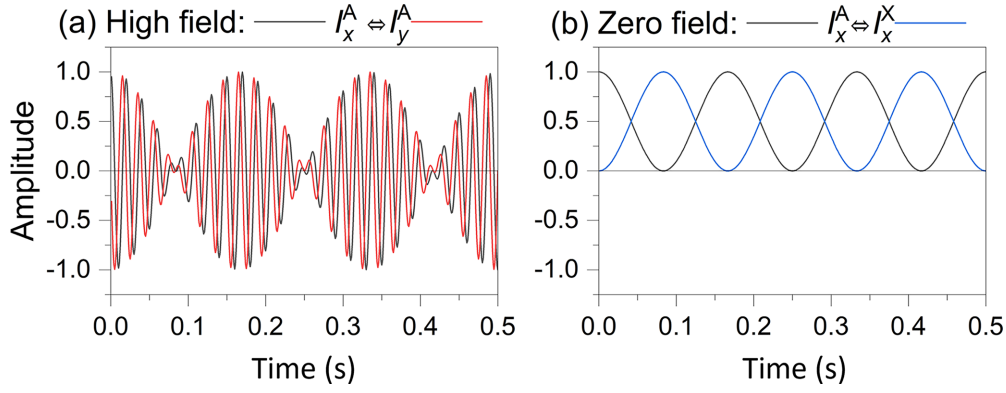
FIG. 3. Evolution of $\hat{I}_x^A$ spin operator at high (a) and zero (b) magnetic fields. At high field, there is precession of magnetization, while at zero field, there is pumping of polarization from one spin to the other along the same direction. Here, we used Eq. (7) with $J = 6$ Hz and $\nu^A = 50$ Hz.

at HF and ZF is as follows:

$$
\hat{I}_x^A \xrightarrow{2\pi \hat{H}(B_0 \to +\infty)t} \frac{1}{2}\left[\cos\left(2\pi\left(\nu^A - \frac{J}{2}\right)t\right) + \cos\left(2\pi\left(\nu^A + \frac{J}{2}\right)t\right)\right]\hat{I}_x^A - \frac{1}{2}\left[\sin\left(2\pi\left(\nu^A - \frac{J}{2}\right)t\right) + \sin\left(2\pi\left(\nu^A + \frac{J}{2}\right)t\right)\right]\hat{I}_y^A
$$

$$
+ \left[\cos\left(2\pi\left(\nu^A - \frac{J}{2}\right)t\right) - \cos\left(2\pi\left(\nu^A + \frac{J}{2}\right)t\right)\right]\hat{I}_x^A\hat{I}_z^X - \left[\sin\left(2\pi\left(\nu^A - \frac{J}{2}\right)t\right) - \sin\left(2\pi\left(\nu^A + \frac{J}{2}\right)t\right)\right]\hat{I}_y^A\hat{I}_z^X
$$

$$
\hat{I}_x^A \xrightarrow{2\pi \hat{H}(B_0 \to 0)t} \cos^2(\pi J t)\hat{I}_x^A + \sin^2(\pi J t)\hat{I}_x^X - \sin(2\pi J t)\left(\hat{I}_z^A\hat{I}_y^X - \hat{I}_y^A\hat{I}_z^X\right)
$$

$$
\hat{I}_z^A \xrightarrow{2\pi \hat{H}(B_0 \to +\infty)t} \hat{I}_z^A
$$

$$
\hat{I}_z^A \xrightarrow{2\pi \hat{H}(B_0 \to 0)t} \cos^2(\pi J t)\hat{I}_z^A + \sin^2(\pi J t)\hat{I}_z^X - \frac{1}{2}\sin(2\pi J t)\left(\hat{I}_y^A\hat{I}_x^X - \hat{I}_x^A\hat{I}_y^X\right), \tag{7}
$$

The evolution of $\hat{I}_x^A$ results in different observables and types in the FID at HF and ZF conditions (Fig. 3). At HF, nuclear spin precesses around the magnetic field in the z direction. At ZF, polarization does not precess and does not change sign, but rather oscillates from spin A to spin X. The other difference between HF and ZF is that at HF, the longitudinal magnetization does not evolve. In contrast, at low fields it does, which is responsible for the observation of the forbidden transition between states 2 and 3.

Then, under the action of the Hamiltonian [Eq. (1)], the density matrix $\hat{\rho}$ of the spin system evolves. Using a magnetic-field detector placed along the x-, y-, and z axes, the FIDs can be acquired. The acquired signal (acq) is proportional to the magnetization of each spin and depends on the observation axis:

$$
\text{acq}_x = \text{Tr}\left(\hat{\rho}(t)\left(\gamma^A\hat{I}_x^A + \gamma^X\hat{I}_x^X\right)\right) \quad \text{acq}_y = \text{Tr}\left(\hat{\rho}(t)\left(\gamma^A\hat{I}_y^A + \gamma^X\hat{I}_y^X\right)\right) \quad \text{acq}_z = \text{Tr}\left(\hat{\rho}(t)\left(\gamma^A\hat{I}_z^A + \gamma^X\hat{I}_z^X\right)\right). \tag{8}
$$

The calculation of the spin evolution of the density matrix given in Eq. (3) results in the following possible signal intensities for the three axes for an arbitrary magnetic field along the z axis:

$$
\begin{aligned}
4\text{acq}_x = {} & \cos(2\pi\nu_{2\to 1}t)\left[p_x^A\sin(\theta) - p_x^X\cos(\theta)\right]\left[\gamma^A\sin(\theta) - \gamma^X\cos(\theta)\right] \\
& + \cos(2\pi\nu_{4\to 2}t)\left[p_x^A\cos(\theta) - p_x^X\sin(\theta)\right]\left[\gamma^A\cos(\theta) - \gamma^X\sin(\theta)\right] \\
& + \cos(2\pi\nu_{4\to 3}t)\left[p_x^A\sin(\theta) + p_x^X\cos(\theta)\right]\left[\gamma^A\sin(\theta) + \gamma^X\cos(\theta)\right] \\
& + \cos(2\pi\nu_{3\to 1}t)\left[p_x^A\cos(\theta) + p_x^X\sin(\theta)\right]\left[\gamma^A\cos(\theta) + \gamma^X\sin(\theta)\right] \\
-4\text{acq}_y = {} & \sin(2\pi\nu_{2\to 1}t)\left[p_x^A\sin(\theta) - p_x^X\cos(\theta)\right]\left[\gamma^A\sin(\theta) - \gamma^X\cos(\theta)\right] \\
& + \sin(2\pi\nu_{4\to 2}t)\left[p_x^A\cos(\theta) - p_x^X\sin(\theta)\right]\left[\gamma^A\cos(\theta) - \gamma^X\sin(\theta)\right] \\
& + \sin(2\pi\nu_{4\to 3}t)\left[p_x^A\sin(\theta) + p_x^X\cos(\theta)\right]\left[\gamma^A\sin(\theta) + \gamma^X\cos(\theta)\right] \\
& + \sin(2\pi\nu_{3\to 1}t)\left[p_x^A\cos(\theta) + p_x^X\sin(\theta)\right]\left[\gamma^A\cos(\theta) + \gamma^X\sin(\theta)\right] \\
4\text{acq}_z = {} & 2\left(p_z^A\gamma^A + p_z^X\gamma^X\right) - \left(p_z^A - p_z^X\right)\left(\gamma^A - \gamma^X\right)\left[1 - \cos(2\pi\nu_{3\to 2}t)\right]\sin^2(2\theta).
\end{aligned} \tag{9}
$$

The corresponding high-field and ZULF approximations are

$$4\mathrm{acq}_x \overset{2\pi\hat{H}(B_0\to+\infty)t}{\rightarrow} p_x^A\gamma^A\left[\cos\left(2\pi\left(\nu^A-\frac{J}{2}\right)t\right)+\cos\left(2\pi\left(\nu^A+\frac{J}{2}\right)t\right)\right]$$

$$+p_x^X\gamma^X\left[\cos\left(2\pi\left(\nu^X-\frac{J}{2}\right)t\right)+\cos\left(2\pi\left(\nu^X+\frac{J}{2}\right)t\right)\right]$$

$$-4\mathrm{acq}_y \overset{2\pi\hat{H}(B_0\to+\infty)t}{\rightarrow} p_x^A\gamma^A\left[\sin\left(2\pi\left(\nu^A-\frac{J}{2}\right)t\right)+\sin\left(2\pi\left(\nu^A+\frac{J}{2}\right)t\right)\right]$$

$$+p_x^X\gamma^X\left[\sin\left(2\pi\left(\nu^X-\frac{J}{2}\right)t\right)+\sin\left(2\pi\left(\nu^X+\frac{J}{2}\right)t\right)\right]$$

$$4\mathrm{acq}_z \overset{2\pi\hat{H}(B_0\to+\infty)t}{\rightarrow} 2\left(p_z^A\gamma^A+p_z^X\gamma^X\right)$$

$$4\mathrm{acq}_x \overset{2\pi\hat{H}(B_0\to0)t}{\rightarrow} \left[(p_x^A+p_x^X)(\gamma^A+\gamma^X)+(p_x^A-p_x^X)(\gamma^A-\gamma^X)\cos(2\pi Jt)\right]\cos\left(2\pi\frac{\Sigma\nu}{2}t\right)$$

$$-4\mathrm{acq}_y \overset{2\pi\hat{H}(B_0\to0)t}{\rightarrow} \left[(p_x^A+p_x^X)(\gamma^A+\gamma^X)+(p_x^A-p_x^X)(\gamma^A-\gamma^X)\cos(2\pi Jt)\right]\sin\left(2\pi\frac{\Sigma\nu}{2}t\right)$$

$$4\mathrm{acq}_z \overset{2\pi\hat{H}(B_0\to0)t}{\rightarrow} \left(p_z^A+p_z^X\right)(\gamma^A+\gamma^X)+\left(p_z^A-p_z^X\right)(\gamma^A-\gamma^X)\cos(2\pi Jt) \tag{10}$$

One can see that the corresponding HF spectrum precisely coincides with a typical HF Zeeman spectrum. This manifests as two transitions for each spin with frequency difference J, signal proportional to both polarization and gyromagnetic ratio, and longitudinal magnetization that does not evolve (note that each spin's polarization and gyromagnetic ratio go together and do not mix). Of note here, quadrature detection (simultaneous detection of acq_x and acq_y) can also be used to add up signals and improve the SNR by $\sqrt{2}$.

At ZULF conditions, acq_z gives a nontrivial spin evolution. At strictly zero fields, only acq_x and acq_z result in observable signals, while acq_y gives no signal at all. Additionally, the signal at the J frequency is only obtained when polarization and gyromagnetic values for the two spins are different. At nonzero fields, acq_y results in two antiphase lines with frequencies $J\pm\frac{\Sigma\nu}{2}$ and one line at $\frac{\Sigma\nu}{2}$. acq_x produces two in-phase lines at $J\pm\frac{\Sigma\nu}{2}$ and one line at $\frac{\Sigma\nu}{2}$. And finally, acq_z, as at zero field, still gives resonances at J and 0. The effect from the longitudinal magnetic field on the J resonance of acq_z is much smaller than on $\mathrm{acq}_{x,y}$ and is $\frac{\delta\nu^2}{2J}\ll\Sigma\nu$ at ZULF conditions. This observation shows that $J\pm\frac{\Sigma\nu}{2}$ offset peaks are what is primarily visible when measuring orthogonal to the magnetic field.

At HF, the coils are even less sensitive to the imperfections, since only acq_x and acq_y are observed. Additionally, these signals differ from one another only by a phase shift, which can be compensated for even during postprocessing. However, this is not the case at ZULF, since all three components result in different acquired signals (assuming $p_y\neq0$), recommending detection along two (quadrature) if not all three axes. Although separating noise from signal [52] and small magnetic-field inhomogeneity $\Sigma\nu\neq0$ (<1 nT, see SM [43]) are further reasons to use quadrature detection, even at ZULF [8], we have not done so, due to having minimized the field

inhomogeneity and the infeasibility of setting up another fully independent SQUID detector in quadrature.

From an experimental perspective, perfect alignment of magnetic-field polarization and orientation in addition to perfect system geometry is unlikely. Therefore, empirical observations are a superposition of the three possible outcomes, whose polarization and magnetic-field orientation can be deduced by applying our solutions [Eq. (10)] to the observed signals.

B. NMR spectra of multiple spins-1/2 at arbitrary magnetic field

The two-spin system is the simplest example of the coupled spin system. The following steps of complexity are A_2X, A_3X, and A_nX (n is any integer) spin systems. Because of the structure of the spin Hamiltonian [Eq. (1)], the analysis of the more complex systems can be reduced to several AX-type spin systems where A is a spin in the range from $n/2$ to 0 for even n and 1/2 for odd n. This is because the spin states of an A_nX system with total spin-I of the A_n subsystem do not mix with the subsystem corresponding to the total spin, $J\neq$I:

$$\hat{\mathrm{H}}^{A_nX}=-\nu^A\sum_{k=1}^{n}\hat{\mathrm{I}}_z^{A_k}-\nu^X\hat{\mathrm{I}}_z^X+J\left(\sum_{k=1}^{n}\hat{\mathbf{I}}^{A_k}\cdot\hat{\mathbf{I}}^X\right)$$

$$=-\nu^A\hat{\mathrm{F}}_z^{A_n}-\nu^X\hat{\mathrm{I}}_z^X+J(\hat{\mathbf{F}}^{A_n}\cdot\hat{\mathbf{I}}^X), \tag{11}$$

where $\hat{\mathbf{F}}^{A_n}=\sum_{k=1}^{n}\hat{\mathbf{I}}^{A_k}$ and $\hat{\mathrm{F}}_z^{A_n}=\sum_{k=1}^{n}\hat{\mathrm{I}}_z^{A_k}$ are the total spin and the corresponding projection of the A_n group of spins. This form of the Hamiltonian shows how it can be written in a block-diagonal form for subsystems with different total spin; hence, each subsystem can be treated independently. Therefore, the A_2X system can be represented as two AX systems, where A has total spin-0 (A^0X system) in one and spin-1 (A^1X system) in the other. The A_3X system can be
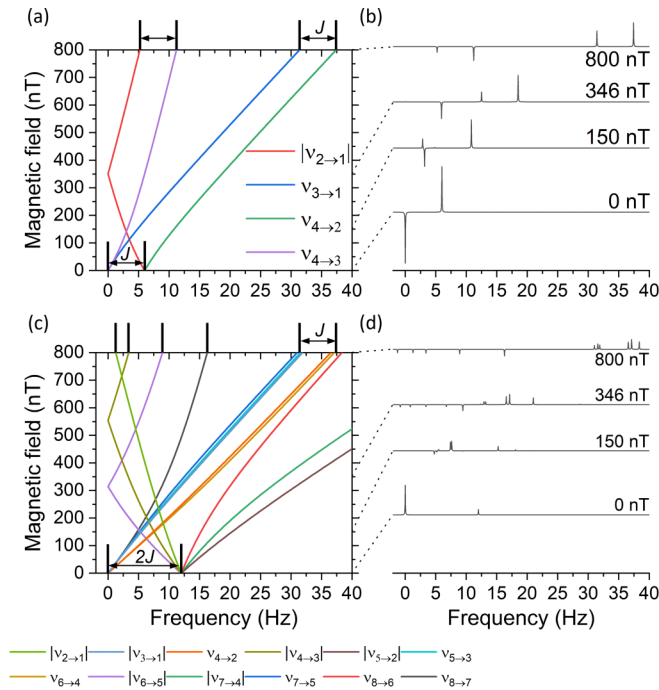
FIG. 4. Simulated frequency transitions and corresponding NMR spectra of the AX and $A^{3/2}X$ systems that comprise the A_3X spin system of 1-Py and 2-Py. System parameters: The A symbol represents the ^{1}H atom and the X symbol represents the ^{13}C, with their corresponding gyromagnetic ratios. In (a), (b) the A spin has spin-1/2 and in (c), (d) spin-3/2. Nuclear-spin polarization was $p_x^A = 0.5$, $p_x^X = -1$, spin-spin interaction was $J = 6$ Hz. The spectra simulate detection along the x axis without relaxation. For the spectra in (b) and (d), the signal was multiplied with $\exp(-Rt)$ with $R = 0.2\,\mathrm{s}^{-1}$, simulating signal decay. The analogous diagram for an A^1X system is shown in the SM [43].

represented with three AX spin systems: one AX system with spin-3/2 ($A^{3/2}X$) and two AX systems with spin-1/2 (AX systems). This approach simplifies the analytical diagonalization of the Hamiltonian for A_nX systems.

The primary focus of this work is the A_3X system, since it represents the spin structure of 1-Py and 2-Py molecules, which will be discussed below. For the sake of completeness, we also give the energy levels for an AX spin system with X being spin-1/2 and A being spin-0 [A^0X or just X, Eq. (S3)], spin-1 [A^1X, Eq. (S9)], and spin-3/2 [$A^{3/2}X$, Eq. (S11)] in the SM [43].

Using these energy levels, one can calculate single quantum transition frequencies, $\nu_{k\to l} = E_k - E_l$; example simulated spectra and transition frequencies illustrate the difference between HF and ZULF spectra for AX and $A^{3/2}X$ systems (Fig. 4).

C. Hyperpolarization of 1-Py and 2-Py, using SABRE-SHEATH

To evaluate these results empirically, we increased the NMR signal by hyperpolarizing 1-Py and 2-Py using SABRE-SHEATH [22] (Fig. 5). Using these isotopically labeled compounds and SABRE-SHEATH allowed us to measure ZULF spectra, since at least two nuclear spins with different

gyromagnetic ratios are necessary for a ZULF acquisition, in this case being supplied by ^{13}C and ^{1}H.

We utilized two approaches to detect the FID signal: excitation with a 90° rf pulse (SQUID system installed at the MPI in Tübingen) and nonadiabatic magnetic-field variation (SQUID system installed at the PTB in Berlin) (detailed in Sec. II, Methods).

At $B_{\mathrm{det}}^z = 38.6\,\mu$T, the ^{1}H and ^{13}C spins are weakly coupled, generating multiplet spectra similar to that observed at HF, ignoring the HF observable phenomenon of chemical shift. In these multiplets, the observed peaks are separated by the J-coupling constant between the ^{13}C and ^{1}H nuclei of the pyruvate molecule, resulting in a quadruplet ^{13}C and doublet ^{1}H signal, separated by 1.27 Hz for 1-Py [Fig. 5(a)] and 6 Hz for 2-Py [Fig. 5(b)]. The difference between these two J-coupling frequencies arises from one fewer bond separating the ^{13}C nucleus from the pyruvate methyl protons: 3 for 1-Py and 2 for 2-Py, leading to stronger coupling.

One can also see the presence of other signals in the 2-Py spectrum at 413 and 414 Hz. These features were well reproduced when the natural abundance of ^{13}C was assumed, leading to signal from [1, 2-^{13}C$_2$]pyruvate. These tiny lines were not observed for 1-Py because of signal overlap. For the signal at 1.644 kHz [negative signals in the ^{1}H spectra, Figs. 5(a) and 5(b)], we attribute this to orthohydrogen, dissolved in the sample, as has been observed before [7].

The optimal B_{hyp} was as expected, temperature dependent [22–25], but significantly shifted to lower fields for 2-Py [Fig. 5(d)] compared to 1-Py [Fig. 5(c)]. This cannot be explained by different exchange rates since the same complexes and conditions are expected to result in hyperpolarization (Fig. 1). We found, however, that if one assumes that 2-Py is primarily polarized in another complex, **C-II**, where pyruvate coordinates in the axial orientation [22], then field dependences can be well reproduced [Fig. 5(d)]. The main reason is that in the **C-I** complex, $J^{\mathrm{HH}} \sim -10.5$ Hz [Fig. 5(e)], while in the **C-II** complex, $J^{\mathrm{HH}} \sim -6.5$ Hz [Fig. 5(f)], which moves the optimal B_{hyp} to lower fields. Although **C-II** is less populated than **C-I,** thermodynamically, 2-Py has a much larger coupling to pH$_2$ in **C-II,** of about 2.7 Hz, versus below 1 Hz in **C-I,** which results in a stronger contribution to the polarization of 2-Py from **C-II** versus from **C-I**. Additionally, as predicted in our simulations of magnetic-field dependence, the exchange rates for both complexes are different [Figs. 5(c) and 5(d)]. This indicates that one should also consider more than one complex for predicting and explaining hyperpolarization with SABRE. Considering these findings, further investigations of 2-Py polarization are warranted.

To observe the evolution of pyruvate's spectra from the HF to the ZULF regime, we repeated the prior experiments, this time varying B_{det}^z, instead of B_{hyp}^x. We also then simulated the spectra, as predicted for 1-Py and 2-Py with each of the B_{det}^z fields (Figs. 6 and 7). In the HF regime of 1-Py, the spectra consist of a quadruplet ^{13}C and an antiphase doublet ^{1}H signal at their respective Larmor frequencies, both predicted by the simulations. Again, an additional negative ^{1}H signal corresponds to dissolved orthohydrogen within the sample, which is detectable at these lower B_{det}^z fields and not taken into account in the simulations.
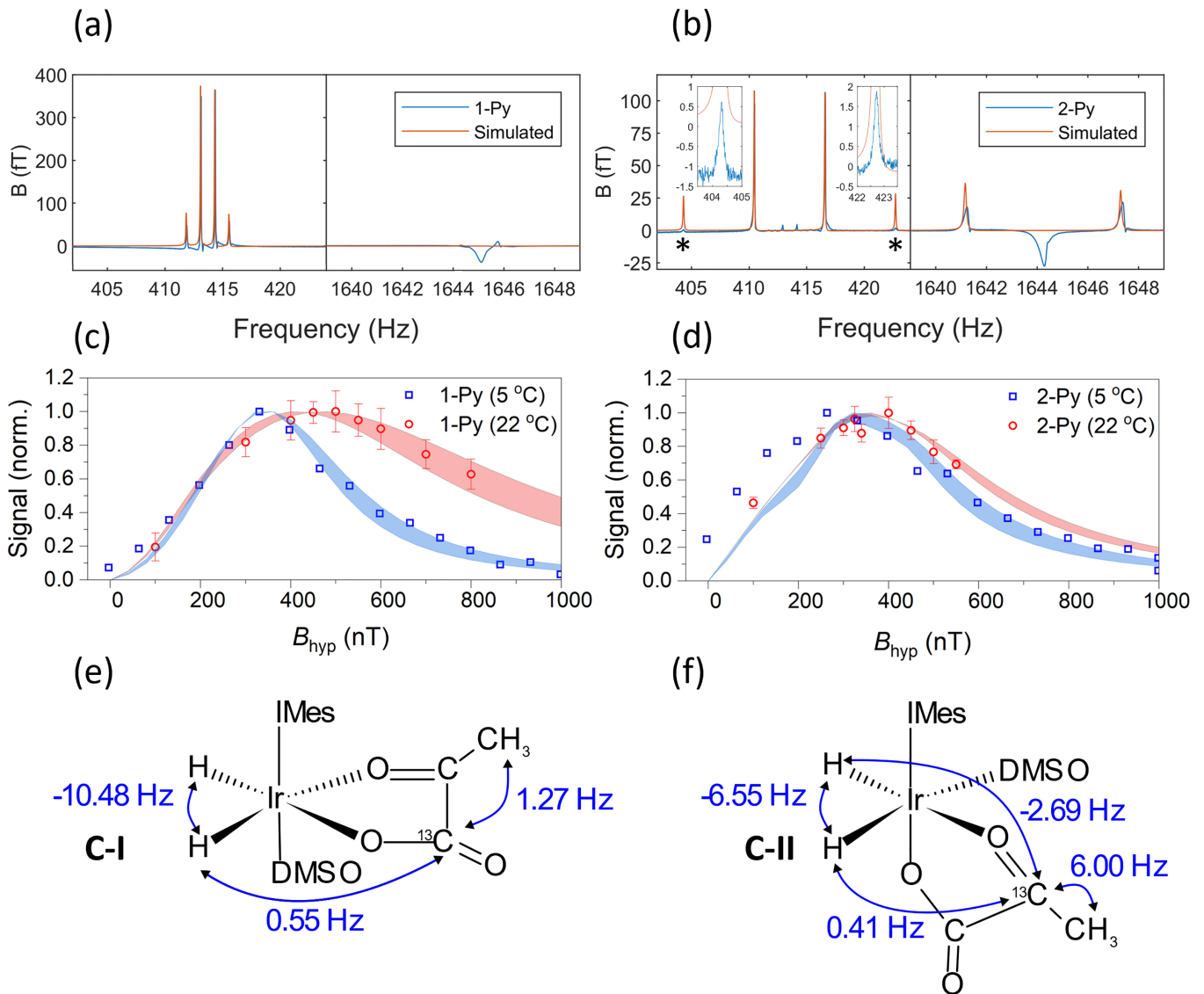
FIG. 5. Low-field spectra of 1-Py and 2-Py and magnetic-field dependence of the ^{13}C SABRE signal. (a) Phased spectra of hyperpolarized 1-Py at $B_{hyp}^x = 500$ nT and 22 °C, acquired at $B_{det}^z = 38.6$ μT along with their simulations. The ^{13}C multiplet is centered around 414 Hz, while the ^{1}H signal is around 1.64 kHz. (b) Phased spectra of hyperpolarized 2-Py at $B_{hyp}^x = 325$ nT and 22 °C, acquired at $B_{det}^z = 38.6$ μT along with their simulations. The peaks around 404 and 423 Hz are marked with an asterisk (*) and shown scaled above for visibility. The dependency of the ^{13}C hyperpolarized 1-Py (c) and 2-Py (d) signal amplitude vs the hyperpolarization field, B_{hyp}^x at 5 °C ($N = 1$, no standard deviation) and at 22 °C ($N \geqslant 5$ with standard deviation). Each experimental and simulated field dependence was independently normalized to 1. All measurements at 22 °C were done at PTB; all measurements at 5 °C were done at MPI. Two pyruvate catalyst complexes **C-I** (e) and **C-II** (f). The following dissociation exchange rates, k_d, were used in the simulations in (c): $85 - 115\,\text{s}^{-1}$ (22 °C) and $30 - 40\,\text{s}^{-1}$ (5 °C), and in (d): $20 - 25\,\text{s}^{-1}$ (22 °C) and $10 - 15\,\text{s}^{-1}$ (5 °C). Simulation details are given in Sec. II, Methods.

As B_{det}^z was decreased, the locations of the signals attributed to ^{13}C and ^{1}H decreased proportional to their respective Larmor frequencies. At a B_{det}^z of approximately 400 nT, the first indicators of the intermediate-coupling regime were both predicted and observed. This manifested initially in splitting of the second and third peaks of the ^{13}C quadruplet into doublets [Fig. 6(a)].

There are slight discrepancies between the simulations and experiments, principally regarding the widths of the predicted and observed peaks and their amplitudes. We propose that the observation of fewer and broader peaks than predicted by

simulations is an incomplete consideration of relaxation in the simulations. Here, we only considered a phenomenological uniform line broadening and included intramolecular dipole-dipole relaxation. More detailed consideration of relaxation mechanisms (detailed below) could then explain how multiple overlapping peaks could be broad and unresolved.

At $B_{det}^z \sim 20$ nT, the peaks eventually evolve into the J-coupling spectrum. For an A_3X system, two peaks are predicted to collapse into a single peak at the J-coupling frequency at zero field [Fig. 4(a)]. However, we observed an additional peak close to the J-coupling frequency starting
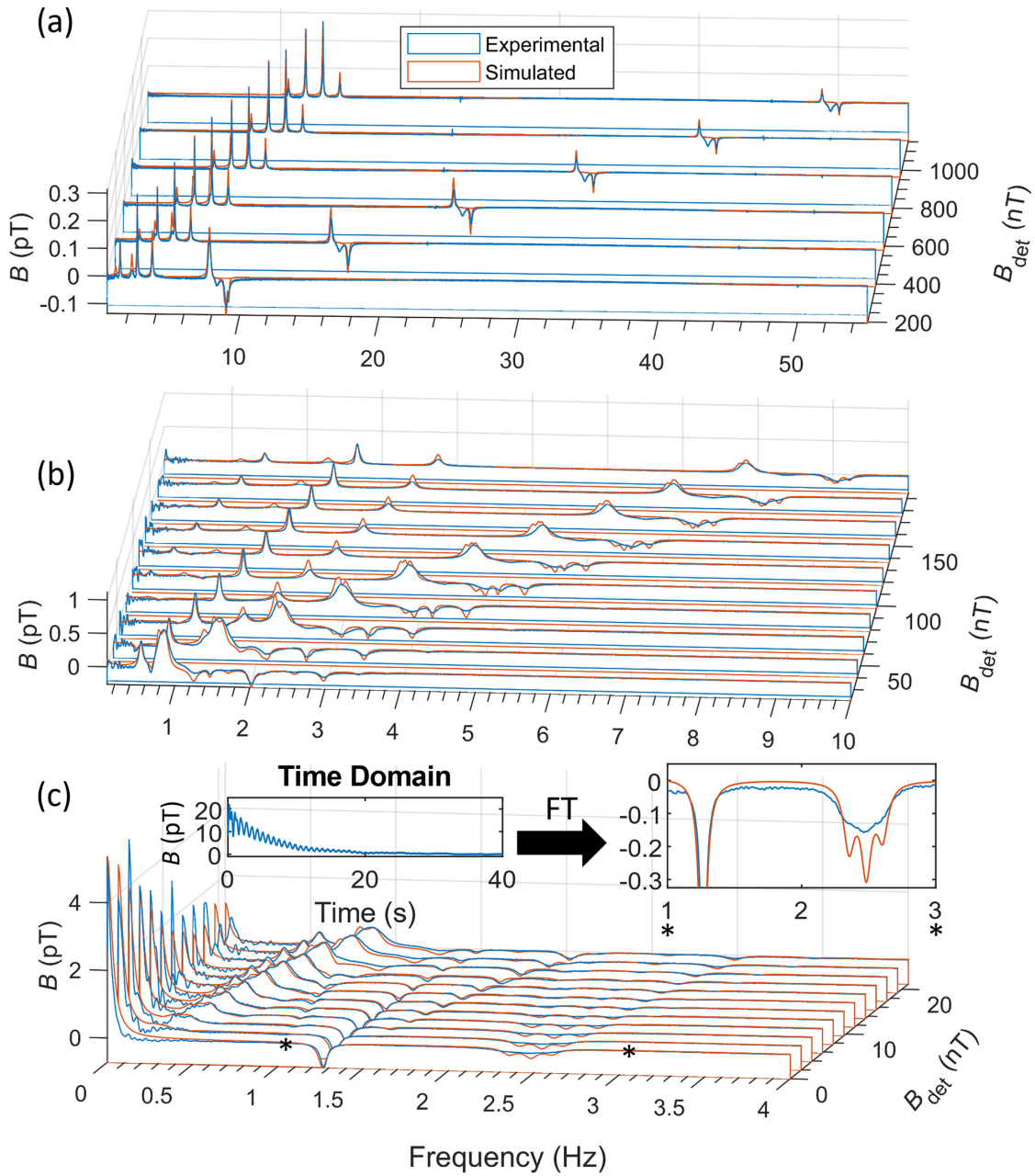
FIG. 6. Experimental and simulated spectra of 1-Py. (a) Spectra from 1 µT to 200 nT. (b) Spectra from 200 to 20 nT. (c) Spectra from 20 nT to ZULF with insets showing the time domain of the ZULF spectrum and its Fourier coefficients between 1–3 Hz. Simulation parameters: $J = 1.223$ Hz, ratio x-polarization X and A nuclei $\frac{p_x^X}{p_x^A} = 5000$, and phenomenological $R = 0.02\,\mathrm{s}^{-1}$.

already at ∼ 20 nT, which can only be predicted in simulations, assuming an additional stray x field in the range of 8 to 13 nT, as a simulation parameter (see geometry of the system in Sec. II, Methods, Fig. 2). We were unable to measure this field by any other means when the reaction chamber was not in place. For instance, measurement of the magnetic field with a fluxgate sensor in the magnetic shield of the applied experimental setup showed field fluctuations in the x direction of less than 1 nT. In addition, the expected demagnetizing field from the sample is on the order of pTs. This leads us to the conclusion that this additional stray x field may well be intrinsic to the sample and requires further investigation.

As the B_{det}^z field was decreased towards the ZULF condition, all signals other than the one at near dc, the J-coupling frequency, and twice the J-coupling frequency went to zero. At ZULF, the time domain of the signal showed an exponentially decaying signal with a periodic element, rather than the usual periodic signal with an exponentially decaying envelope, characteristic of FIDs at high field. This exponential decay results in the near-dc peak after Fourier transform and comes from relaxation of the total polarization of the systems [Eq. (10)]. This observation was also supported by the simulations, which also predicted a large, near-dc peak, with signals at J and $2J$ of the opposite sign to this near-dc peak.
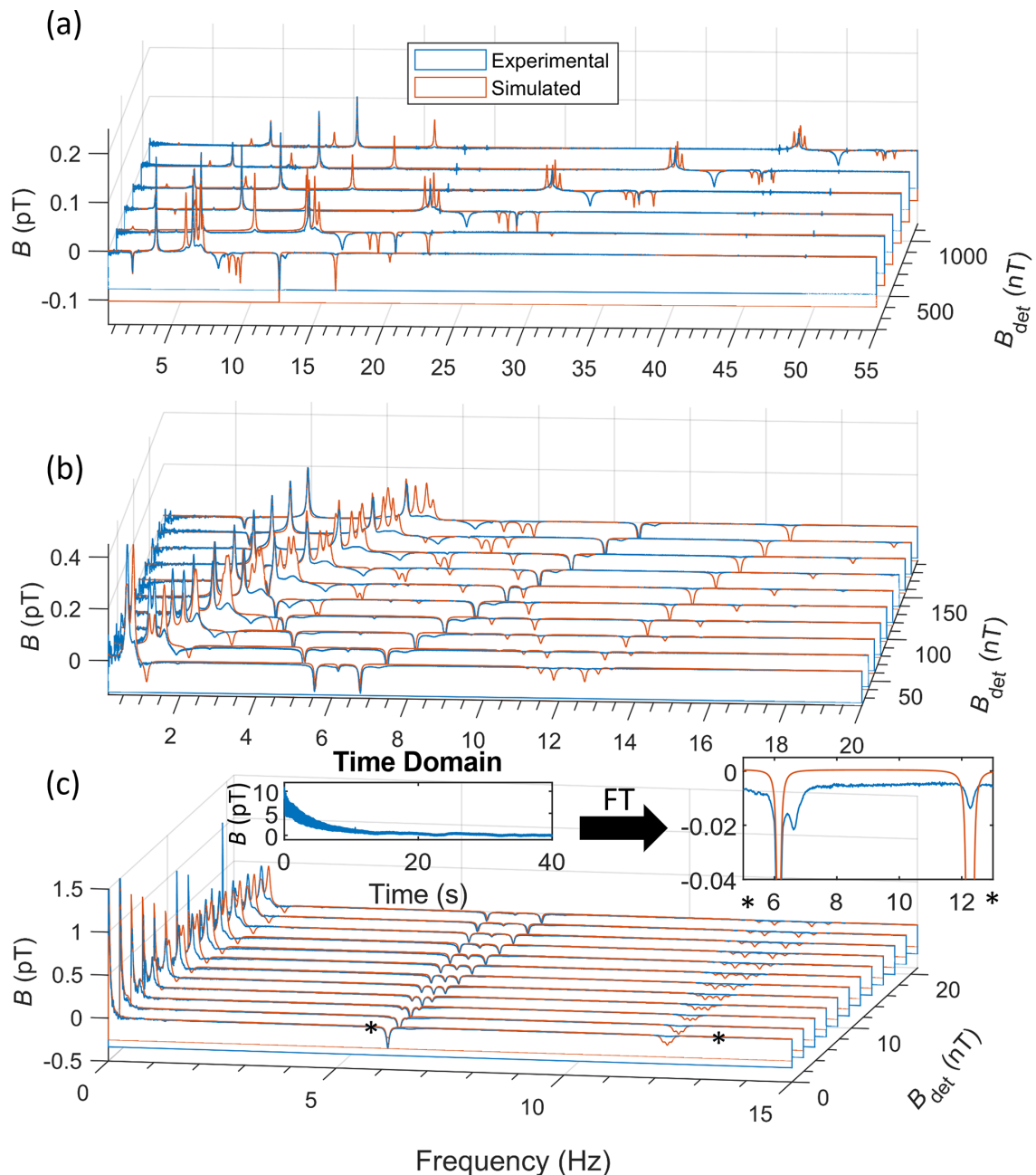
FIG. 7. Experimental and simulated spectra of 2-Py. (a) Spectra from 1 μT to 200 nT. (b) Spectra from 200 to 20 nT. (c) Spectra from 20 nT to ZULF, showing the time domain of the ZULF spectrum and its Fourier coefficients between 5–13 Hz. Simulation parameters: $J = 6.13$ Hz, ratio x-polarization X and A nuclei $\frac{p_x^X}{p_x^A} = 33$, and phenomenological $R = 0.025\,\mathrm{s}^{-1}$.

However, as was observed previously in the intermediate-coupling regime, instead of three peaks centered at $2J$ as predicted by the simulation, only one, broad, lower-amplitude peak across the entire bandwidth of the predicted multiplet was observed. This contrasts with both the amplitudes and structures of the near-dc and J peaks being in agreement in both simulation and observation [Fig. 6(c)].

In contrast to 1-Py, even at a $B_{\mathrm{det}}^z = 1.2$ μT, 2-Py is already clearly in the intermediate-coupling regime. Empirically, this manifests most clearly in the much smaller amplitude of the peak at 9 Hz versus the one at 15 Hz [Fig. 7(a)]. At a $B_{\mathrm{det}}^z = 38.6$ μT (HF regime), these peaks corresponded to the two

central peaks of a ^{13}C quadruplet, which were roughly equivalent in amplitude [Fig. 5(a)]. For the simulations, the same formalism as for 1-Py was used, setting $J = 6.13$ Hz, $\frac{p_x^X}{p_x^A} = 33$, phenomenological $R = 0.025\,\mathrm{s}^{-1}$, and a constant stray x field of 6 nT to allow for direct comparison with the 1-Py simulations. This likely contributed to the increased discrepancies between the simulations and experiments for 2-Py vs. 1-Py, where the simulations predicted peaks that were not observed. For example, the simulations consistently predicted doublets further split into triplets at the ^{1}H signal. However, only an antiphase doublet was experimentally observed. Similar to 1-Py, some of this discrepancy may possibly be due to
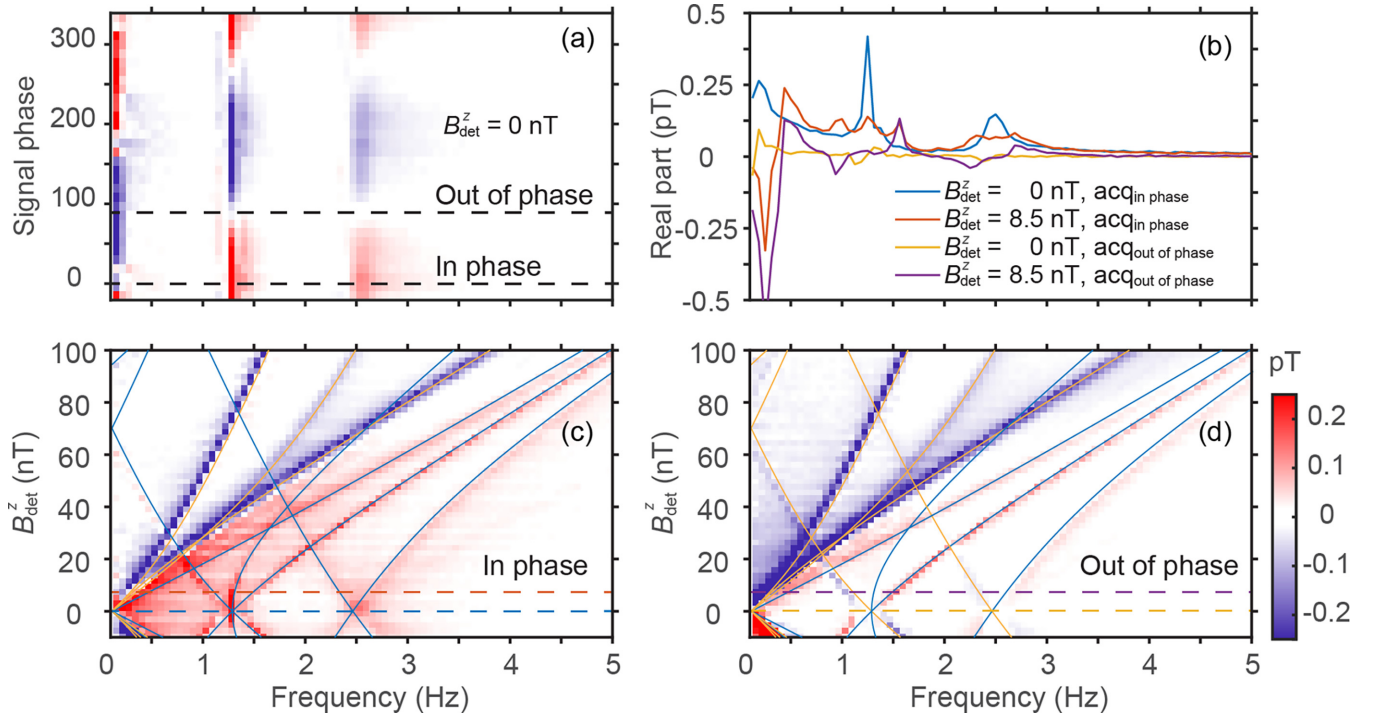
FIG. 8. B_{det}^z and B_1^y phase of rf pulse dependency of 1-Py hyperpolarized by SABRE-SHEATH, acquired with setup at MPI. (a) Measured zero-field spectra (real part of Fourier coefficients) at $B_{det}^z = 0$ nT as a function of B_1^y phase of an rf excitation pulse. (b) Measured selected in-phase and antiphase spectra at $B_{det}^z = 0$ and 8.5 nT. (c) Measured in-phase spectra, and (d) measured antiphase spectra as a function of the B_{det}^z field. The solid lines indicate the simulated position of resonances (red positive and blue negative peaks). The four dashed lines indicate the position of the spectra in (b). The color legend for (a), (c), and (d) is shown to the right of (d). The signal detection acq$_x$ was carried out in the x direction.

unaccounted-for relaxation mechanisms, which is supported by the non-Lorentzian behavior of the bases of the ^{1}H signals. Namely, the widths at the bases of the signals are wider than would be predicted by a Lorentzian fit for the rest of the signal, possibly supporting the presence of additional signals with high relaxation rates.

Similar to 1-Py, as B_{det}^z was decreased, the locations of the ^{13}C and ^{1}H signals also decreased proportional to their Larmor frequencies. However, unlike with 1-Py, at a B_{det}^z of 200 nT, a negative signal at 2.5 Hz already emerges from the near dc that will eventually evolve into a component of the J-frequency signal at ZULF. This difference, where the weak- vs intermediate-coupling regime applies for 1-Py and 2-Py, arises as a direct result of the increased J coupling from 1.27 to 6 Hz [Fig. 4(a)].

As B_{det}^z was further decreased, the signal that evolves into the main component of the J signal at ZULF is clearly visible at ~ 7.7 Hz at a B_{det}^z of 150 nT [Fig. 7(b)] and with different analysis even at higher fields up to 500 nT, which cannot be explained solely by a stray x field in the model (Fig. S6 [43]). Regarding this, at lower fields an additional stray x field, here 6 nT, was required to reproduce this feature in simulations. We also reiterate that we find it unlikely that this is of instrumental origin and speculate that it is inherent to the sample.

Starting at a $B_{det}^z \sim 20$ nT, the 2-Py system is already in the strong-coupling regime, which was not the case for 1-Py until $B_{det}^z \sim 5$ nT. Both simulations and experimental observations

show that as B_{det}^z is decreased from 20 nT to ZULF, the near-dc peak gradually evolves and the triplet around J gradually merges into a single negative peak at the J frequency in the ZULF spectrum [Fig. 7(c)].

Spectra from ZF to ULF have previously been observed using OPMs [8]. However, due to limitations in sensitivity, OPMs are suitable for measurements only at a frequency below a few hundred Hz [8,10], although OPMs operating at kHz frequencies are available [53]. SQUIDs have no such limitations, allowing us to measure NMR spectra from 0 to >1.5 kHz (note that the top frequency was far from the limits of the hardware).

D. Observation angle for ZULF spectra

As predicted for an AX spin system [Eq. (10)], the orientation of the signal acquisition (acq) or observation axis with respect to magnetic field and polarization was also very important, especially at $B_0 = 0$. To demonstrate this effect, we used a sequence, where we could tweak the axis of polarization with respect to signal acquisition direction, acq$_x$, in the xy plane (see sequence details in SM [43]; note that the direction of corresponding signal acquisition is indicated with subscripts). The intensity of the peaks at J and $2J$ follows a sinusoidal behavior as a function of signal phase [Fig. 8(a)]. The maximum intensity appears when the polarization of the initial state is parallel or antiparallel to acq$_x$ (in phase). When the polarization is perpendicular to acq$_x$ (parallel to the y
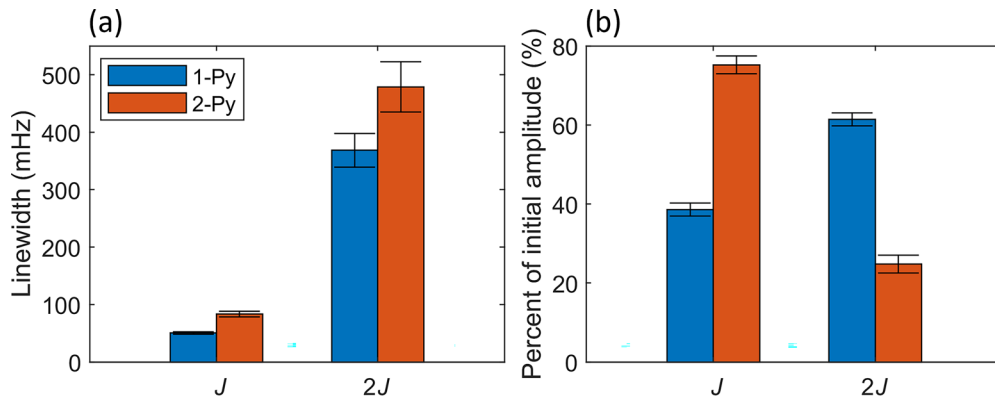
FIG. 9. Linewidths and magnetization distribution of J and $2J$ signals at ZULF. Full width at half maximums for signals at J and $2J$ are shown for 1-Py and 2-Py. The magnetization distribution between the two signals is shown via the percentage of the summed J and $2J$ signals for each molecule ($N \geqslant 3$, standard deviation shown in error bars).

axis, out of phase), there is almost no observable signal, confirming theoretical expectations [Eqs. (10), (S21), and (S22), SM [43]].

This can be appealingly explained by spins, which are oscillating in the direction of polarization with the J and $2J$ frequencies instead of precessing. By applying a small disturbance field, B_{det}^{z}, the oscillation along one axis is overlaid by spin precession transversal to the magnetic-field plane. This is illustrated with four typical experimental spectra at $B_{\mathrm{det}}^{z} = 0$ and 8.5 nT [Fig. 8(b)].

For a small nonzero magnetic field, the peaks at J and $2J$ split into an in-phase doublet when signal is observed in phase and an antiphase doublet when the signal is observed out of phase. These doublets are caused by single quantum coherence transitions.

In addition, there is again a middle peak (still at J), which one expects to be at a forbidden transition at high field [Eq. (10)], but as discussed before allowed at ZULF and near ZULF. Note that this forbidden transition is visible only in the in-phase spectra (no middle peak at J or $2J$ is observable for out-of-phase signal acquisition) as expected.

The B_{det}^{z} dependency of the spectra up to 100 nT is demonstrated in Figs. 8(c) and 8(d) for in phase and out of phase acquisition of spectra, respectively. The simulated transition frequencies [solid lines in Figs. 8(c) and 8(d)] were calculated from the energy eigenvalues in Eq. (S7) and Eq. (S11) [43]; $J = 1.2$ Hz was assumed in the calculus. These frequencies are in good agreement with the predictions we made using simplified AX and $A^{3/2}X$ systems [Figs. 2, 8(c), and 8(d)].

E. T_2 relaxation of pyruvate at ZULF

Another observed feature is that the J and $2J$ peaks of both 1-Py and 2-Py have different linewidths [Fig. 9(a)]. The J peak was about 5–10 times narrower than the $2J$ peak, making the latter harder to observe as its amplitude decreased. Previously, similar spectra have been obtained for 2-Py hyperpolarized, using dissolution dynamic nuclear polarization [6]. At higher fields, the outer peaks of the ^{13}C quadruplet were observed to be broader than the two inner peaks, which has already been

observed in literature, but not previously discussed [54]. One can see that the outer peaks of the ^{13}C quadruplet correspond to the spin state of ^{13}C-labeled pyruvate with a total spin of 2; the same spin states correspond to the signals at $2J$. More detailed relaxation simulation and analysis, including measurement of relaxation as a function of the magnetic field, should shed light on this phenomenon.

One consequence of this phenomenon is how the total magnetization of the sample is distributed between the J and $2J$ peaks. Due to the much larger linewidth of the $2J$ peak the apparent size of the $2J$ signal is much smaller than the J signal (Figs. 6 and 7), even when they are of similar strength at the start of acquisition [Fig. 9(b)]. This highlights that spin-2 is more exposed to the additional relaxation mechanisms than spin-1. Understanding the mechanisms behind this would be useful, since pyruvate has *in vivo* applications, and one should find the optimal conditions for hyperpolarization and storage of hyperpolarization before utilization. A similar discrepancy between predicted relaxation and observed relaxation has also been discussed by Eills *et al.* [8]. We tried to reproduce the difference in linewidths, using the intramolecular dipole-dipole relaxation mechanism and the Redfield relaxation theory approach [44], which did not provide satisfactory agreement with observations.

We think that one should likely consider molecular dynamics, including chemical exchange of the carboxyl proton and interactions with methanol [55]. For example, there is slow chemical exchange of pyruvate with methanol that at low magnetic fields can accelerate nuclear-spin relaxation [56]. Such effects in some extreme cases have been shown to lead to complete polarization loss [57]. The relaxation rate in this mechanism is proportional to $I(I + 1)$ [54], resulting in a 3 times stronger relaxation contribution to spin-2 versus to spin-1. However, this does not completely explain the difference of a factor 5–10 observed in the linewidths of the J and $2J$ peaks [Fig. 9(a)]. For a more precise analysis, one would also need to consider this relaxation mechanism for the composite spin of the A_3X system in conjunction with: intermolecular dipole-dipole interactions with the solvent in addition to another relaxation mechanism. These factors would be necessary to

be able to identify the leading relaxation sources and to reproduce the faster relaxation of pyruvate with total spin of 1 and 2 [58–60].

IV. CONCLUSION

The SQUID setup has allowed us to measure ^{1}H and ^{13}C hyperpolarized signals of 1-Py and 2-Py in magnetic fields from 0 to 100 μT, covering the frequency range from near dc to about 5 kHz. The high sensitivity permitted us to track the spin systems at this range of magnetic fields with exclusive resolution below 30 mHz. We also demonstrated the difference in product-operator evolution at high field versus zero field and showed how crucial it is to orient the magnetometer correctly with regards to the residual magnetic field and orientation of magnetization. Although there is always spin evolution at zero field (if the system is polarized), one can only observe it if the sensor is aligned with the magnetization since the spins are oscillating along the polarization axis with the *J*-coupling frequency, instead of precessing in a plane. Due to spin precession at high fields, the acquisition direction is not particularly important as long as the sensor is positioned orthogonal to the magnetic field. Using our product-operator formulation, we were able to discriminate signals coming from different orientations of polarization at ZULF.

Additionally, with our setup, we were able to achieve high enough signal resolution and field homogeneity to find the relaxation of the different spin states of pyruvate to be significantly different for spin manifolds with total spin-1 and -2 with accelerated relaxation for spin-2, also meriting further theoretical and experimental investigation. This illustrates the

applications and complemented insights to the spin systems that the ZULF systems can provide [61,62].

Our characterization of 1-Py and 2-Py has shown the utility of an ultrasensitive SQUID setup, backed with an understanding of spin evolution, for the continued investigation of magnetic resonance phenomena.

More detailed calculation of the product-operator evolution, eigenvalues, and eigenstates for other spin systems and experimental details are given in the SM [43]. The MOIN-library [63] script that we used to simulate the ZULF spectra is provided, together with the library (.zip).

[1] A. Haase, J. Frahm, D. Matthaei, W. Hänicke, and K.-D. Merboldt, FLASH imaging: Rapid NMR imaging using low flip-angle pulses, J. Magn. Reson. **213**, 533 (1986).

[2] S. J. Nelson *et al.*, Metabolic imaging of patients with prostate cancer using hyperpolarized [1-^{13}C]pyruvate, Sci. Transl. Med. **5**, 198ra108 (2013).

[3] E. Luchinat, L. Barbieri, M. Cremonini, and L. Banci, Protein in-cell NMR spectroscopy at 1.2 GHz, J. Biomol. NMR **75**, 97 (2021).

[4] Q. Liu, S. Liu, Y. Luo, and X. Han, Pulsed-field nuclear magnetic resonance: Status and prospects, Matter Radiat. At Extremes **6**, 024201 (2021).

[5] T. Theis, M. P. Ledbetter, G. Kervern, J. W. Blanchard, P. J. Ganssle, M. C. Butler, H. D. Shin, D. Budker, and A. Pines, Zero-field NMR enhanced by parahydrogen in reversible exchange, J. Am. Chem. Soc. **134**, 3987 (2012).

[6] D. A. Barskiy *et al.*, Zero-field nuclear magnetic resonance of chemically exchanging systems, Nat. Commun. **10**, 3002 (2019).

[7] K. Buckenmaier *et al.*, Multiple quantum coherences hyperpolarized at ultra-low fields, ChemPhysChem **20**, 2823 (2019).

[8] J. Eills *et al.*, Enzymatic reactions observed with zero- and low-field nuclear magnetic resonance, Anal. Chem. **95**, 17997 (2023).

[9] P. Put, S. Alcicek, O. Bondar, Ł. Bodek, S. Duckett, and S. Pustelny, Detection of pyridine derivatives by SABRE hyperpolarization at zero field, Commun. Chem. **6**, 131 (2023).

[10] E. T. Van Dyke, J. Eills, R. Picazo-Frutos, K. F. Sheberstov, Y. Hu, D. Budker, and D. A. Barskiy, Relayed hyperpolarization for zero-field nuclear magnetic resonance, Sci. Adv. **8**, eabp9242 (2022).

[11] J. H. Ardenkjær-Larsen, B. Fridlund, A. Gram, G. Hansson, L. Hansson, M. H. Lerche, R. Servin, M. Thaning, and K. Golman, Increase in signal-to-noise ratio of >10,000 times in liquid-state NMR, Proc. Natl. Acad. Sci. USA **100**, 10158 (2003).

[12] R. W. Adams, J. A. Aguilar, K. D. Atkinson, M. J. Cowley, P. I. P. Elliott, S. B. Duckett, G. G. R. Green, I. G. Khazal, J. López-Serrano, and D. C. Williamson, Reversible interactions with para-hydrogen enhance NMR sensitivity by polarization transfer, Science **323**, 1708 (2009).

[13] J. R. Birchall *et al.*, Batch-mode clinical-scale optical hyperpolarization of xenon-129 using an aluminum jacket with rapid temperature ramping, Anal. Chem. **92**, 4309 (2020).

[14] S. J. Blundell, Spin-polarized muons in condensed matter physics, Contemp. Phys. **40**, 175 (1999).

[15] K. Buckenmaier *et al.*, Mutual benefit achieved by combining ultralow-field magnetic resonance and hyperpolarizing techniques, Rev. Sci. Instrum. **89**, 125103 (2018).

[16] W. Myers, D. Slichter, M. Hatridge, S. Busch, M. Mößle, R. McDermott, A. Trabesinger, and J. Clarke, Calculated signal-to-noise ratio of MRI detected with SQUIDs and Faraday detectors in fields from 10 µT to 1.5T, J. Magn. Reson. **186**, 182 (2007).

[17] Ya. S. Greenberg, Application of superconducting quantum interference devices to nuclear magnetic resonance, Rev. Mod. Phys. **70**, 175 (1998).

[18] D. Budker and M. Romalis, Optical magnetometry, Nat. Phys. **3**, 227 (2007).

[19] R. Körber *et al.*, SQUIDs in biomagnetism: A roadmap towards improved healthcare, Supercond. Sci. Technol. **29**, 113001 (2016).

[20] B. Inglis, K. Buckenmaier, P. SanGiorgio, A. F. Pedersen, M. A. Nichols, and J. Clarke, MRI of the human brain at 130 microtesla, Proc. Natl. Acad. Sci. USA **110**, 19194 (2013).

[21] P. J. Rayner, M. J. Burns, A. M. Olaru, P. Norcott, M. Fekete, G. G. R. Green, L. A. R. Highton, R. E. Mewis, and S. B. Duckett, Delivering strong ^{1}H nuclear hyperpolarization levels and long magnetic lifetimes through signal amplification by reversible exchange, Proc. Natl. Acad. Sci. USA **114**, E3188 (2017).

[22] W. Iali, S. S. Roy, B. J. Tickner, F. Ahwal, A. J. Kennerley, and S. B. Duckett, Hyperpolarising pyruvate through signal amplification by reversible exchange (SABRE), Angew. Chem. Int. Ed. **58**, 10271 (2019).

[23] B. J. Tickner, O. Semenova, W. Iali, P. J. Rayner, A. C. Whitwood, and S. B. Duckett, Optimisation of pyruvate hyperpolarisation using SABRE by tuning the active magnetisation transfer catalyst, Catal. Sci. Technol. **10**, 1343 (2020).

[24] P. TomHon, M. Abdulmojeed, I. Adelabu, S. Nantogma, M. S. H. Kabir, S. Lehmkuhl, E. Y. Chekmenev, and T. Theis, Temperature cycling enables efficient ^{13}C SABRE-SHEATH hyperpolarization and imaging of [1-^{13}C]-pyruvate, J. Am. Chem. Soc. **144**, 282 (2022).

[25] I. Adelabu *et al.*, Rapid ^{13}C hyperpolarization of the TCA cycle intermediate α-ketoglutarate via SABRE-SHEATH, Anal. Chem. **94**, 13422 (2022).

[26] T. Theis, M. L. Truong, A. M. Coffey, R. V. Shchepin, K. W. Waddell, F. Shi, B. M. Goodson, W. S. Warren, and E. Y. Chekmenev, Microtesla SABRE enables 10% nitrogen-15 nuclear spin polarization, J. Am. Chem. Soc. **137**, 1404 (2015).

[27] M. Fekete, F. Ahwal, and S. B. Duckett, Remarkable levels of 15N polarization delivered through SABRE into unlabeled pyridine, pyrazine, or metronidazole enable single scan NMR quantification at the mM level, J. Phys. Chem. B **124**, 4573 (2020).

[28] M. J. Cowley, R. W. Adams, K. D. Atkinson, M. C. R. Cockett, S. B. Duckett, G. G. R. Green, J. A. B. Lohman, R. Kerssebaum, D. Kilgour, and R. E. Mewis, Iridium N-heterocyclic carbene complexes as efficient catalysts for magnetization transfer from para-hydrogen, J. Am. Chem. Soc. **133**, 6134 (2011).

[29] A. N. Pravdivtsev, A. V. Yurkovskaya, H.-M. Vieth, K. L. Ivanov, and R. Kaptein, Level anti-crossings are a key factor

[30] for understanding para-hydrogen-induced hyperpolarization in SABRE experiments, ChemPhysChem **14**, 3327 (2013).

[30] R. W. Adams, S. B. Duckett, R. A. Green, D. C. Williamson, and G. G. R. Green, A theoretical basis for spontaneous polarization transfer in non-hydrogenative parahydrogen-induced polarization, J. Chem. Phys. **131**, 194505 (2009).

[31] S. Knecht, A. N. Pravdivtsev, J.-B. Hövener, A. V. Yurkovskaya, and K. L. Ivanov, Quantitative description of the SABRE process: Rigorous consideration of spin dynamics and chemical exchange, RSC Adv. **6**, 24470 (2016).

[32] S. L. Eriksson, J. R. Lindale, X. Li, and W. S. Warren, Improving SABRE hyperpolarization with highly nonintuitive pulse sequences: Moving beyond avoided crossings to describe dynamics, Sci. Adv. **8**, eabl3708 (2022).

[33] A. N. Pravdivtsev and J.-B. Hövener, Coherent polarization transfer in chemically exchanging systems, Phys. Chem. Chem. Phys. **22**, 8963 (2020).

[34] K. MacCulloch *et al.*, Facile hyperpolarization chemistry for molecular imaging and metabolic tracking of [1-^{13}C]pyruvate in vivo, J. Magn. Reson. Open **16**, 100129 (2023).

[35] H. de Maissin *et al.*, In vivo metabolic imaging of [1-^{13}C]pyruvate-D3 hyperpolarized by reversible exchange with parahydrogen, Angew. Chem. Int. Ed. **62**, e202306654 (2023).

[36] M. P. Ledbetter, C. W. Crawford, A. Pines, D. E. Wemmer, S. Knappe, J. Kitching, and D. Budker, Optical detection of NMR J-spectra at zero magnetic field, J. Magn. Reson. **199**, 25 (2009).

[37] T. Theis, P. Ganssle, G. Kervern, S. Knappe, J. Kitching, M. P. Ledbetter, D. Budker, and A. Pines, Parahydrogen-enhanced zero-field nuclear magnetic resonance, Nat. Phys. **7**, 571 (2011).

[38] M. P. Ledbetter, T. Theis, J. W. Blanchard, H. Ring, P. Ganssle, S. Appelt, B. Blümich, A. Pines, and D. Budker, Near-zero-field nuclear magnetic resonance, Phys. Rev. Lett. **107**, 107601 (2011).

[39] M. C. Butler, M. P. Ledbetter, T. Theis, J. W. Blanchard, D. Budker, and A. Pines, Multiplets at zero magnetic field: The geometry of zero-field NMR, J. Chem. Phys. **138**, 184202 (2013).

[40] T. Theis, J. W. Blanchard, M. C. Butler, M. P. Ledbetter, D. Budker, and A. Pines, Chemical analysis using J-coupling multiplets in zero-field NMR, Chem. Phys. Lett. **580**, 160 (2013).

[41] J.-H. Storm, P. Hömmen, D. Drung, and R. Körber, An ultra-sensitive and wideband magnetometer based on a superconducting quantum interference device, Appl. Phys. Lett. **110**, 072603 (2017).

[42] J. Voigt, S. Knappe-Grüneberg, D. Gutkelch, J. Haueisen, S. Neuber, A. Schnabel, and M. Burghoff, Development of a vector-tensor system to measure the absolute magnetic flux density and its gradient in magnetically shielded rooms, Rev. Sci. Instrum. **86**, 055109 (2015).

[43] See Supplemental Material at http://link.aps.org/supplemental/10.1103/PhysRevB.109.184443 for the derivation of energy levels from the Hamiltonian for other spin systems, the setup at the MPI, spectra between 1.5−38.6 µT, and more analysis of the central *J* peak from Figs. 6 and 7.

[44] J. Kowalewski and L. Mäler, *Nuclear Spin Relaxation in Liquids: Theory, Experiments, and Applications* (Taylor & Francis, Boca Raton, 2006).

[45] K. Ivanov, A. Yurkovskaya, and H.-M. Vieth, High resolution NMR study of T1 magnetic relaxation dispersion. I. Theoretical

considerations of relaxation of scalar coupled spins at arbitrary magnetic field, J. Chem. Phys. **129**, 234513 (2008).

[46] A. N. Pravdivtsev, K. L. Ivanov, R. Kaptein, and A. V. Yurkovskaya, Theoretical study of dipolar relaxation of coupled nuclear spins at variable magnetic field, Appl. Magn. Reson. **44**, 23 (2013).

[47] A. N. Pravdivtsev, I. V. Skovpin, A. I. Svyatova, N. V. Chukanov, L. M. Kovtunova, V. I. Bukhtiyarov, E. Y. Chekmenev, K. V. Kovtunov, I. V. Koptyug, and J.-B. Hovener, Chemical exchange reaction effect on polarization transfer efficiency in SLIC-SABRE, J. Phys. Chem. A **122**, 9107 (2018).

[48] C. D. Assaf, X. Gui, A. A. Auer, S. B. Duckett, J.-B. Hövener, and A. N. Pravdivtsev, J coupling constants of <1 Hz enable ^{13}C hyperpolarization of pyruvate via reversible exchange of parahydrogen, J. Phys. Chem. Lett. **15**, 1195 (2024).

[49] L. D. Vázquez-Serrano, B. T. Owens, and J. M. Buriak, Catalytic olefin hydrogenation using N-heterocyclic carbene–phosphine complexes of iridium, Chem. Commun. **21**, 2518 (2002).

[50] Q. Stern and K. Sheberstov, Simulation of NMR spectra at zero and ultralow fields from A to Z − a tribute to Professor Konstantin L'vovich Ivanov, Magn. Reson. **4**, 87 (2023).

[51] O. W. Sørensen, G. W. Eich, M. H. Levitt, G. Bodenhausen, and R. R. Ernst, Product operator formalism for the description of NMR pulse experiments, Prog. Nucl. Magn. Reson. Spectrosc. **16**, 163 (1984).

[52] M. Jiang, R. P. Frutos, T. Wu, J. W. Blanchard, X. Peng, and D. Budker, Magnetic gradiometer for the detection of zero- to ultralow-field nuclear magnetic resonance, Phys. Rev. Appl. **11**, 024005 (2019).

[53] I. Savukov, Y. J. Kim, V. Shah, and M. G. Boshier, High-sensitivity operation of single-beam optically pumped magnetometer in a kHz frequency range, Meas. Sci. Technol. **28**, 035104 (2017).

[54] A. N. Pravdivtsev, K. Buckenmaier, N. Kempf, G. Stevanato, K. Scheffler, J. Engelmann, M. Plaumann, R. Koerber, J.-B. Hövener, and T. Theis, LIGHT-SABRE hyperpolarizes

$1 - {}^{13}$C-pyruvate continuously without magnetic field cycling, J. Phys. Chem. C **127**, 6744 (2023).

[55] A. Svyatova, V. P. Kozinenko, N. V. Chukanov, D. B. Burueva, E. Y. Chekmenev, Y.-W. Chen, D. W. Hwang, K. V. Kovtunov, and I. V. Koptyug, PHIP hyperpolarized [1-^{13}C]pyruvate and [1-^{13}C]acetate esters via PH-INEPT polarization transfer monitored by 13 C NMR and MRI, Sci. Rep. **11**, 5646 (2021).

[56] E. Chiavazza, E. Kubala, C. V. Gringeri, S. Düwel, M. Durst, R. F. Schulte, and M. I. Menzel, Earth's magnetic field enabled scalar coupling relaxation of ^{13}C nuclei bound to fast-relaxing quadrupolar 14N in amide groups, J. Magn. Reson. **227**, 35 (2013).

[57] J. P. Peters *et al.*, Nitrogen-15 dynamic nuclear polarization of nicotinamide derivatives in biocompatible solutions, Sci. Adv. **9**, eadd3643 (2023).

[58] G. Pileio, M. Carravetta, E. Hughes, and M. H. Levitt, The long-lived nuclear singlet state of 15N-nitrous oxide in solution, J. Am. Chem. Soc. **130**, 12582 (2008).

[59] G. Stevanato, J. T. Hill-Cousins, P. Håkansson, S. S. Roy, L. J. Brown, R. C. D. Brown, G. Pileio, and M. H. Levitt, A nuclear singlet lifetime of more than one hour in room-temperature solution, Angew. Chem. Int. Ed. **54**, 3740 (2015).

[60] G. Pileio, M. Carravetta, and M. H. Levitt, Storage of nuclear magnetization as long-lived singlet order in low magnetic field, Proc. Natl. Acad. Sci. USA **107**, 17135 (2010).

[61] J. W. Blanchard, T. F. Sjolander, J. P. King, M. P. Ledbetter, E. H. Levine, V. S. Bajaj, D. Budker, and A. Pines, Measurement of untruncated nuclear spin interactions via zero- to ultralow-field nuclear magnetic resonance, Phys. Rev. B **92**, 220202(R) (2015).

[62] S. Alcicek, P. Put, A. Kubrak, F. C. Alcicek, D. Barskiy, S. Gloeggler, J. Dybas, and S. Pustelny, Zero- to low-field relaxometry of chemical and biological fluids, Chem. Commun. **6**, 165 (2023).

[63] A. N. Pravdivtsev and J.-B. Hövener, Simulating non-linear chemical and physical (CAP) dynamics of signal amplification by reversible exchange (SABRE), Chem. Eur. J. **25**, 7659 (2019).